Three-level DC-DC GaN-based Converter with Active Thermal Control for Powertrain applications in Electric Vehicles

Rubén González[1], Christian A. Rojas[1], Leonardo Callegaro[2]
[1]*Electronics Engineering Department, Universidad Técnica Federico Santa María*, Valparaíso, Chile
[2]*School of Engineering, Macquarie University*, Sydney, NSW, Australia
ruben.gonzalez.13@sansano.usm.cl, c.a.rojas@ieee.org, leonardo.callegaro@mq.edu.au

2021 22nd IEEE International Conference on Industrial Technology (ICIT) | 978-1-7281-5730-6/20/$31.00 ©2021 IEEE | DOI: 10.1109/ICIT46573.2021.9453595

***Abstract*—The use of electric vehicles (EVs) has grown notably in the last years and with it new challenges for power electronics have appeared. Since typically the main energy storage system in EVs consists of batteries, one of these challenges is the efficient and reliable management of power flows in charging/discharging mode. This paper presents an electrical and thermal modelling of a three-level buck-boost DC-DC converter (TLBBC) with semiconductors based on gallium nitride (GaN) technology. Also an active thermal control (ATC) scheme to mitigate the thermal stress in the semiconductor is proposed, together with control schemes for DC-link voltage and voltage balance between capacitors in the TLBBC. The TLBBC is designed to operate in a boost mode at rated power of 25 kW, using a parallel design with GaN semiconductors. Proposed control schemes are implemented using linear controllers. Finally, comprehensive simulation results confirm and validate the proposed control schemes.**

***Index Terms*—Active Thermal Control (ATC), DC-DC converter, Gallium Nitride (GaN), Three-level buck-boost converter (TLBBC), Voltage Balance Control (VBC).**

I. Introduction

NOWADAYS, due to the need to use more sustainable and less polluting energy, use of electric transport has grown considerably. This is reflected in an increasing number of electric vehicles (EVs) within the automotive fleet worldwide [1]. In a parallel way, power electronics had been developed to solve the new challenges given by these new technologies, such as building high-power charging station and developing fast chargers and power converters [2], [3].

Relevant applications of power electronics in EVs are in the powertrain, which typically consists of a battery pack as energy storage system, a bidirectional DC-DC converter, an DC-AC inverter and an electric motor, as shown in Fig. 1. The bi-directional DC-DC converter is used to manage energy and power flows between the battery and the DC-link of the inverter. This converter also should boost the low battery voltage up to the high DC-link voltage of the inverter in the motor driving mode, and needs to charge the battery with the regenerative energy for vehicle deceleration and braking.

Different topologies can be used to implement the DC-DC converter, which are able to manage power flow between the battery and powertrain in an EV, such as Interleaved boost, Three-level Flying capacitor boost and Three-level boost [4]. From the topologies proposed in the literature, the three-level buck-boost DC-DC converter (TLBBC) is a good alternative, because it has lower voltage stress in the semiconductors compared to two-level topologies, and uses fewer switches compared to others three-level topologies [4].

Choosing adequate semiconductors for a converter is not an easy task, because important features as efficiency, power density or voltage ratio depend on them. Under this context, recently developed Gallium Nitride High Electron Mobility Transistors (GaN HEMTs) are being applied in many high-power electronic devices, because their better performance and advantages, such as close to zero switching-off losses and higher power density compared to conventional Si MOSFETs [5]. Despite the above mentioned advantages, the bigger limitation of GaN devices is their breakdown voltage, although it is currently increasing from 650 V [6], 900 V [7] and 1200 V [8]. Power level limitations can be solved using serial-parallel design, which allows to achieve higher power level [9].

Otherwise, the DC-DC converter must be able to ensure a controlled voltage level in DC-link when battery delivers power to the powertrain [10]. Furthermore, to guarantee an equal voltage distribution between the output capacitors in the TLBBC, a voltage balance control (VBC) strategy is needed [11]. Thermal stress is another critical issue for electrical devices, and therefore also for semiconductors, since it affects strongly their lifetime and performance [12]. Hence, applying an active thermal control (ATC) strategy to ensure a safe thermal operating point has a very high relevance [12]–[15]. An adequate thermal model is also relevant to implement an effective ATC, such as in [14], where a power loss modelling and thermal behaviour for a GaN-based converter are analyzed. Thermal control can be achieved with different strategies, such as in [15], where an ATC is applied to a GaN-based DC-DC converter, which controls the devices slew rates through

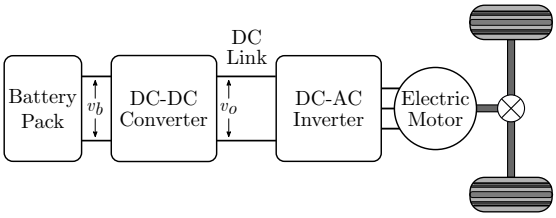

Fig. 1: Diagram of a powertrain in EVs.

the use of a two-step gate driver. In contrast, in this paper a detailed thermal modelling of the system is performed, and an ATC strategy based on varying the switching frequency of the converter to regulate the operation temperature is proposed.

This paper is organized as follows. Section II presents a comprehensive electrical and thermal modelling of the TLBBC under study. Section III proposes first-order models and control schemes including output voltage control, VBC and ATC. Section IV shows simulation results. Conclusion and future work are presented in Section V.

II. System Modelling

A. Topology Description and Operation Principle

Powertrain DC-DC converter can achieve high power level using a parallel connection between n modules as shown in Fig. 2a [16]. This paper focuses on studying one of these modules, whose topology corresponds to a TLBBC as shown in Fig. 2b. The topology consists in four switches S_1, S_2, S_3, S_4, an input filter composed of a distributed inductor L_b and capacitor C_b, and an output filter composed of two capacitors C_1 and C_2. In this case, each switch represents two GaN HEMT semiconductors connected in parallel in order to achieve a higher power level [9], [17]. Using GaN devices as switches, the TLBBC can operate as bi-directional converter, but in this paper only the boost mode is analyzed, so switches S_2 and S_3 are used to control it.

To guarantee a correct behavior and prevent short circuit, gate signals of the outer switches S_1 and S_4 must operate complementary to their adjacent inner switches S_2 and S_3. Gate signals are generated by phase-shift pulse width modulation (PS-PWM), with a 180° shift between both signals and variable frequency. Dead time implementation is also needed to ensure a safe switching operation. Average modulation signals are represented by two duty cycles, d_1 to control S_1 and S_2, and d_2 to control S_3 and S_4. The TLBBC average model considers an operation in continuous conduction mode (CCM). Output capacitors C_1 and C_2 are assumed to be large enough so that the output voltage $v_o = v_{c1} + v_{c2}$ is assumed to be constant during the entire switching cycle. Furthermore, thermal dynamics are assumed to be much slower than electrical dynamics, so this allows a decoupled thermal controller design from electrical controller design and therefore, the switching frequency given from thermal control can be considered as constant in the average electrical model.

B. Average Converter Model

Considering that duty cycles d_1 and d_2 are the control inputs to the TLBBC, the switching cycle averaged state equations for the circuit shown in Fig. 2b are

$$\frac{di_b}{dt} = \frac{v_b}{L_b} - \frac{(1-d_1)}{L_b}v_{c1} - \frac{(1-d_2)}{L_b}v_{c2} \tag{1}$$

$$\frac{dv_{c1}}{dt} = \frac{(1-d_1)}{C_1}i_b - \frac{i_o}{C_1} \tag{2}$$

$$\frac{dv_{c2}}{dt} = \frac{(1-d_2)}{C_2}i_b - \frac{i_o}{C_2} \tag{3}$$

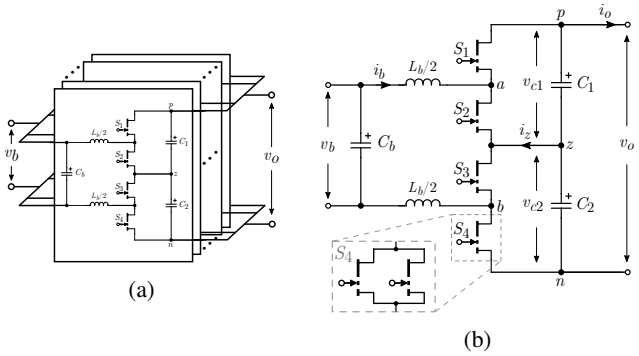

Fig. 2: Three-level buck-boost DC-DC converter: a) parallel connection of n modules. b) topology of one module.

where the inductor current i_b and capacitor voltages v_{c1} and v_{c2} are the state variables. The input voltage v_b and output current i_o are assumed to be constant.

A small-signal linearization of (1)-(3) about an operating point can be written in the state-space form as

$$\begin{cases} \dot{\tilde{\boldsymbol{x}}} &= \mathbf{A}\tilde{\boldsymbol{x}} + \mathbf{B}\tilde{\boldsymbol{u}} \\ \tilde{\boldsymbol{y}} &= \mathbf{C}\tilde{\boldsymbol{x}} + \mathbf{D}\tilde{\boldsymbol{u}} \end{cases} \tag{4}$$

where the state vector is $\tilde{\boldsymbol{x}} = [\tilde{i}_b\ \tilde{v}_{c1}\ \tilde{v}_{c2}]^T$, the input vector is $\tilde{\boldsymbol{u}} = [\tilde{d}_1\ \tilde{d}_2]^T$, and to control the inductor current, difference between capacitor voltages $\Delta\tilde{v}_c = \tilde{v}_{c1} - \tilde{v}_{c2}$, and output voltage, the three-dimensional output vector $\tilde{\boldsymbol{y}} = [\tilde{i}_b\ \Delta\tilde{v}_c\ \tilde{v}_o]^T$ is required. Carrying out the mathematical analysis, the matrix of the linearized model are

$$\begin{cases} \mathbf{A} = \begin{bmatrix} 0 & -\frac{1-D_1}{L_b} & -\frac{1-D_2}{L_b} \\ \frac{1-D_1}{C_1} & 0 & 0 \\ \frac{1-D_2}{C_2} & 0 & 0 \end{bmatrix} & \mathbf{B} = \begin{bmatrix} \frac{V_{C1}}{L_b} & \frac{V_{C2}}{L_b} \\ -\frac{I_b}{C_1} & 0 \\ 0 & -\frac{I_b}{C_2} \end{bmatrix} \\ \mathbf{C} = \begin{bmatrix} 1 & 0 & 0 \\ 0 & 1 & -1 \\ 0 & 1 & 1 \end{bmatrix} & \mathbf{D} = \begin{bmatrix} 0 & 0 \\ 0 & 0 \\ 0 & 0 \end{bmatrix} \end{cases} \tag{5}$$

note that uppercase letters denote the value at the operating point. Finally, with the matrix model defined in (5), the continuous time model can be obtained using the well-known transfer function matrix

$$\mathbf{G}(s) = \mathbf{C}(s\mathbf{I} - \mathbf{A})^{-1}\mathbf{B} + \mathbf{D} \tag{6}$$

where $\mathbf{I}$ is a 3x3 identity matrix.

C. Thermal Model

Thermal model considers that GaN devices are connected to the heatsink through an Insulated Metal Substrate (IMS) board with homogeneous behavior. IMS board is selected because its good thermal performance compared to Fibreglass resin (FR4) PCB [18]. Connection and proposed thermal model based on a Cauer-type RC thermal network, including the junction-to-case RC thermal model of GaN devices, and RC thermal model of solder, IMS board, thermal grease and heatsink is shown in Fig. 3. Current source P_{Loss} in junction-to-case RC thermal model, represents power losses of GaN device, which consist

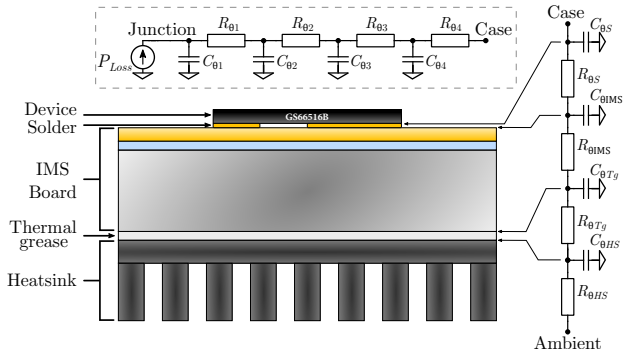

Fig. 3: Thermal model between junction and ambient temperature.

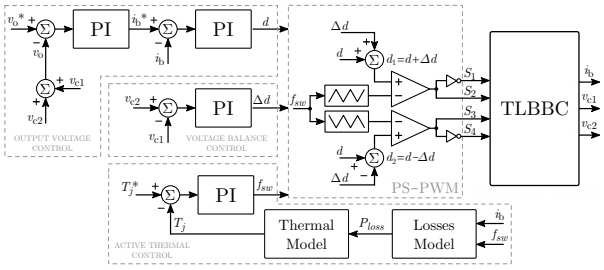

Fig. 4: Complete control scheme.

of two parts, conduction losses and switching losses. In this work, P_{Loss} is obtained through simulation in PLECS with a provided power loss model by GaN Systems [19].

Given the difficulty of measuring junction temperature, it can be estimated with a state-space model considering the temperatures of thermal capacities as state-variables, and considering as inputs the power losses P_{Loss}, and case temperature T_c. The state-space model based on thermal RC junction-to-case thermal circuit shown in Fig. 3 can be defined as

$$\frac{dx_1}{dt} = -\frac{1}{C_{\theta 1}R_{\theta 1}}x_1 + \frac{1}{C_{\theta 1}R_{\theta 1}}x_2 + \frac{1}{C_{\theta 1}}P_{Loss} \tag{7}$$

$$\frac{dx_2}{dt} = \frac{1}{C_{\theta 2}R_{\theta 1}}x_1 - \frac{R_{\theta 1}+R_{\theta 2}}{C_{\theta 2}R_{\theta 1}R_{\theta 2}}x_2 + \frac{1}{C_{\theta 2}R_{\theta 2}}x_3 \tag{8}$$

$$\frac{dx_3}{dt} = \frac{1}{C_{\theta 3}R_{\theta 2}}x_2 - \frac{R_{\theta 2}+R_{\theta 3}}{C_{\theta 3}R_{\theta 2}R_{\theta 3}}x_3 + \frac{1}{C_{\theta 3}R_{\theta 3}}x_4 \tag{9}$$

$$\frac{dx_4}{dt} = \frac{1}{C_{\theta 4}R_{\theta 3}}x_3 - \frac{R_{\theta 3}+R_{\theta 4}}{C_{\theta 4}R_{\theta 3}R_{\theta 4}}x_4 + \frac{1}{C_{\theta 4}R_{\theta 4}}T_c \tag{10}$$

here, state variable x_1 represents junction temperature T_j.

III. System Control

Control objectives are inductor current, capacitors voltage balance, output voltage and junction temperature. The complete proposed control scheme is shown in Fig. 4. The continuous time model in (6) can be expressed in a matrix form

$$\begin{bmatrix} \tilde{i}_b \\ \Delta\tilde{v}_c \\ \tilde{v}_o \end{bmatrix} = \begin{bmatrix} Gi_bd_1 & Gi_bd_2 \\ G_\Delta v_c d_1 & G_\Delta v_c d_2 \\ Gv_o d_1 & Gv_o d_2 \end{bmatrix} \begin{bmatrix} \tilde{d}_1 \\ \tilde{d}_2 \end{bmatrix} \tag{11}$$

this representation is useful to identify the transfer functions to control. To implement the control systems, this paper proposes the use of PI controllers. The controllers design considers that transfer functions must approximate the first-order form $\frac{1}{\tau s}$, where τ is a time constant. From closed loop analysis, values of integral and constant gains can be expressed as

$$K_i = \omega_{BW}^2 \left(\sqrt{(1+2\xi^2)^2+1} - (1+2\xi^2)\right)\tau \tag{12}$$

$$K_p = 2\xi\sqrt{\tau K_i} \tag{13}$$

where ω_{BW} is the bandwidth and ξ is the damping coefficient, both are defined as design parameters.

Otherwise, at the operating point, capacitor voltages are expected to be balanced, $V_{c1} = V_{c2} = V_c = V_o/2$, and both capacitance values supposed to be identical, $C_1 = C_2 = C$. Furthermore, both duty cycles are expected to be equal, and defined as $D_1 = D_2 = D$.

A. Current Control

Transfer functions between duty cycle and inductor current, from (11) can be expressed and approximated as

$$Gi_bd_x = \frac{\tilde{i}_b}{\tilde{d}_x} = \frac{sCV_c + I_b(1-D)}{s^2CL_b + 2(1-D)^2} \overset{C\to\infty}{\approx} \frac{V_c}{sL_b} \tag{14}$$

here x = {1,2}, because the expression is identical for $\tilde{d}_1$ and $\tilde{d}_2$. This allows to employ just one controller to obtain signal d, which contributes directly on d_1 and d_2, as shown in Fig. 4. Approximated form can be considered because capacitance values are assumed to be large enough so that their voltages are assumed to be constant during the entire switching cycle.

B. Voltage Balance Control

Transfer functions between duty cycles and capacitors voltage difference, from (11) can be expressed as

$$G_\Delta v_c d_1 = \frac{\Delta\tilde{v}_c}{\tilde{d}_1} = -\frac{I_b}{sC} \tag{15}$$

$$G_\Delta v_c d_2 = \frac{\Delta\tilde{v}_c}{\tilde{d}_2} = \frac{I_b}{sC} \tag{16}$$

Note that (16) at the operating point can be controlled with the same PI controller used for (15), just adding a negative unit gain on the output. This controller generates signal Δd, which contributes directly on d_1, and in a negative way on d_2, as shown in Fig. 4.

C. Output Voltage Control

Control of the output voltage is possible using a cascade control scheme to define a value of current reference as shown in Fig. 4. It is necessary to consider that current control loop is faster than voltage control loop, so the dynamic of the internal current loop can be disregarded when designing the outer voltage loop controller, and the inductor current can be consider as an input to define a new transfer function Gv_oi_b [20]. This transfer function can be obtained from (11), and approximated to the fist-order as follows

$$Gv_oi_b = \frac{Gv_od_x}{Gi_bd_x} = \frac{\tilde{v}_o}{\tilde{i}_b} \approx \frac{2(1-D)}{sC} \tag{17}$$

here x = {1,2}, because the expression is identical for $\tilde{d}_1$ and $\tilde{d}_2$. This allows to employ just one controller to obtain reference value for i_b.

D. Thermal Control

Thermal control is proposed to regulate the junction temperature T_j of the critical switches. Due to the boost operation mode of the converter, the critical switches are the inner semiconductors S_2 and S_3 in the TLBBC. Furthermore, due to the symmetrical operation between S_2 and S_3, a natural thermal balance between them is expected, hence for thermal control loop is sufficient to measure or estimate the temperature of only one of these switches. A relationship between junction temperature, output power of the converter and switching frequency, obtained through simulation, is shown in Fig. 5. It shows that junction temperature has a nonlinear behaviour when varying output power at fixed switching frequency, and has a linear behaviour when varying switching frequency at fixed output power. Fig. 6 shows these previous described behaviours. For that reason, the alternative chosen in this paper to control the junction temperature is varying the switching frequency, considering that converter operates at rated power.

Otherwise, to avoid a complex mathematical analysis to obtain an expression for a complete thermal model of the system, fitting a first-order model as (18), based on a simulation step response is an adequate approximation and sufficient to achieve the objective of this work.

$$G_{T_j f_{sw}} = \frac{T_j}{f_{sw}} = \frac{K_{th}}{\tau_{th} s + 1} \tag{18}$$

Considering the parameters shown in Table I and reducing the case-to-ambient RC model shown in Fig. 3 as a single RC thermal model with $R_{\theta CA} = 0.8\ \frac{^\circ C}{W}$ and $C_{\theta CA} = 0.1\ \frac{W \cdot s}{^\circ C}$ [17], parameters $K_{th} = 8.16 \cdot 10^{-4}$ °C·s and $\tau_{th} = 0.16535$ s for first-order thermal model have been obtained.

IV. Simulation Results

The TLBBC under study with the proposed control schemes and modulation is simulated using PLECS, including GaN thermal models. For validation, a 25 kW converter is designed considering the parameters shown in Table II, and implementing two parallel GS66516B [6] GaN HEMT for each switch. Table III resumes the PI parameters obtained from expressions (12) and (13), and implemented in simulation.

In order to verify the proposed output voltage control, a step response test considering a variation of ± 50 V about operating V_o value is carried out. Fig. 7 shows the effectiveness of proposed output voltage control. Furthermore, to verify the proposed VBC, a 100 Ω resistor is connected parallel to the

TABLE I: Junction to case RC thermal parameters

	Material	$R_{\theta x}$ (°C/W)	$C_{\theta x}$ (Ws/°C)
#1	GaN	0.006	$9.03 \cdot 10^{-5}$
#2	Si	0.125	0.00629
#3	Attachment	0.126	0.00141
#4	Cu base	0.013	0.00214

TABLE II: Simulation parameters

Components		Operating point	
Parameter	Value	Parameter	Value
L_b	2 mH	V_b	400 V
C_b	600 μF	I_b	62.5 A
C_1	1200 μF	V_c	400 V
C_2	1200 μF	V_o	800 V
S_1, S_2, S_3, S_4	2xGS66516B	D	0.5

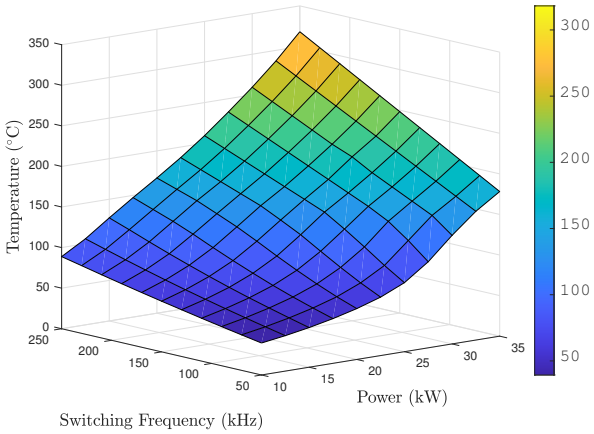

Fig. 5: Three-dimension surface of junction temperature with different switching frequency and output power.

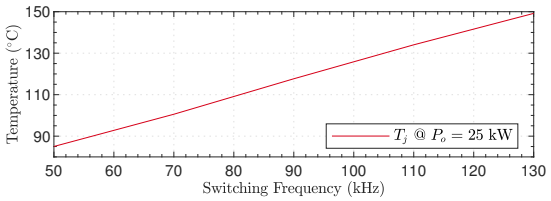

(a)

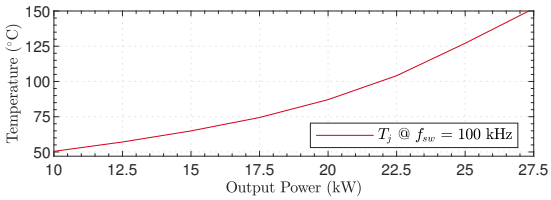

(b)

Fig. 6: Simulated result for dependence of junction temperature by: a) switching frequency at fixed output power of 25 kW. b) output power at fixed switching frequency of 100 kHz.

TABLE III: PI controllers parameters

Control loop	ω_{BW} (rad/s)	ξ (-)	K_p	K_i
i_b	$2\pi 1000$	0.8	0.023	41.385
Δv_c	$2\pi 100$	0.8	-0.009	-1.589
v_o	$2\pi 100$	0.8	0.552	99.324
T_j	$2\pi 25$	1.4	$0.283 \cdot 10^5$	$5.030 \cdot 10^5$

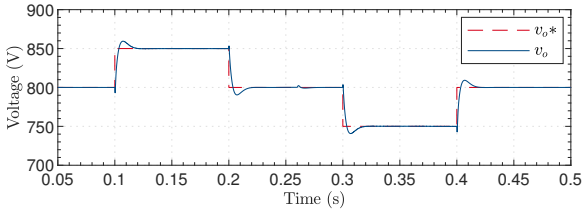

Fig. 7: Simulated results for output voltage control.

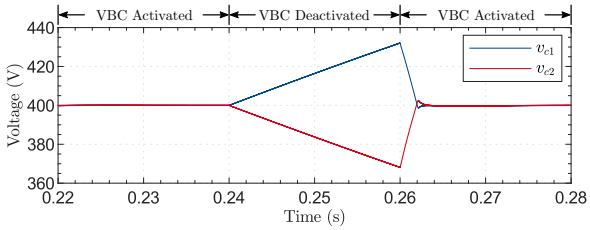

Fig. 8: Simulated results for voltage balance control with a 100 Ω resistor connected parallel to capacitor C_2.

lower capacitor C_2. VBC is activated all the time except the period from 0.24 s to 0.26 s. Fig. 8 shows the effectiveness of proposed VBC, and can be seen that voltage values converge quickly after the VBC activation and keep balanced afterwards.

Otherwise, the complete system is simulated considering an output power profile with variations between 0.5 and 1.0 p.u. Fig. 9 shows effectiveness of both proposed control schemes. Considering the critical operation, when output power decreases to 50% of rated value, the variation of output voltage is not greater than 5%, and balance is achieved all the time.

Proposed thermal control is also tested with the same power profile. First, a test with ATC deactivated is carried out and results are shown in Fig. 10. Due to the ATC is deactivated, a fixed switching frequency of 100 kHz is selected for this test. Results demonstrate that junction temperature has a large variation, which reaches a thermal difference approximately of 60°C when output power decreases to 50% of rated value. Afterwards, a test with ATC activated is carried out and results are shown in Fig. 11. For this test, junction temperature reference is set at 100°C. Simulation results show effectiveness of proposed ATC, which keeps the value of reference temperature with a maximal variation less than 5°C when output power decreases to 50% of rated value. Comparing results in Figs. 10 and 11 is possible to notice the effectiveness of proposed ATC, since the junction temperature keeps reference value. Note that temperature scale presented in Figs. 10 and 11 is not the same, to clearly show the junction temperature variation.

Finally, Fig. 12 shows steady state values for relevant electrical and thermal variables based on circuit in Fig. (2b), demonstrating a correct operation of the complete control scheme. Variables shown are converter voltage v_{ab}, output voltage v_o, inductor current i_b, capacitor voltages v_{c1} and v_{c2}, neutral point current i_z, junction temperature T_j and switching frequency f_{sw}. Simulated results from Fig. 12 also show that voltage and current ripples are much less than 1%, neutral

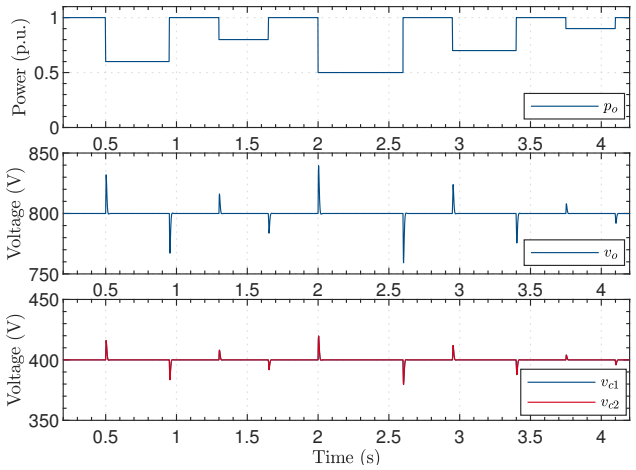

Fig. 9: Simulated results for output voltage and voltage balance.

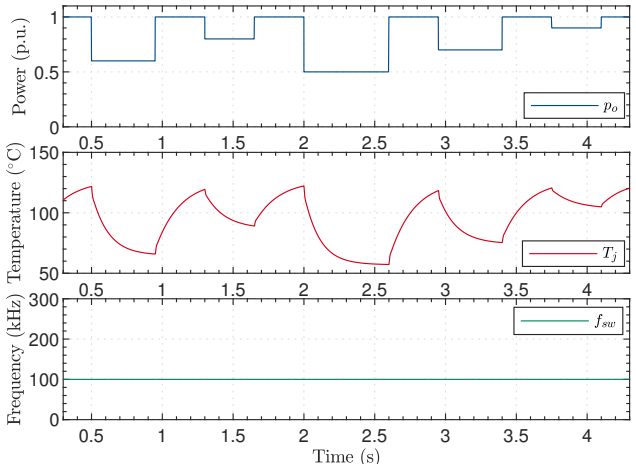

Fig. 10: Simulated result for junction temperature and switching frequency without active thermal control.

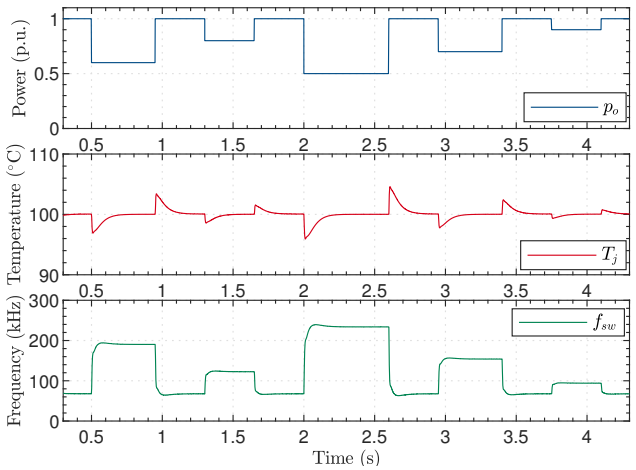

Fig. 11: Simulated result for junction temperature and switching frequency with active thermal control.

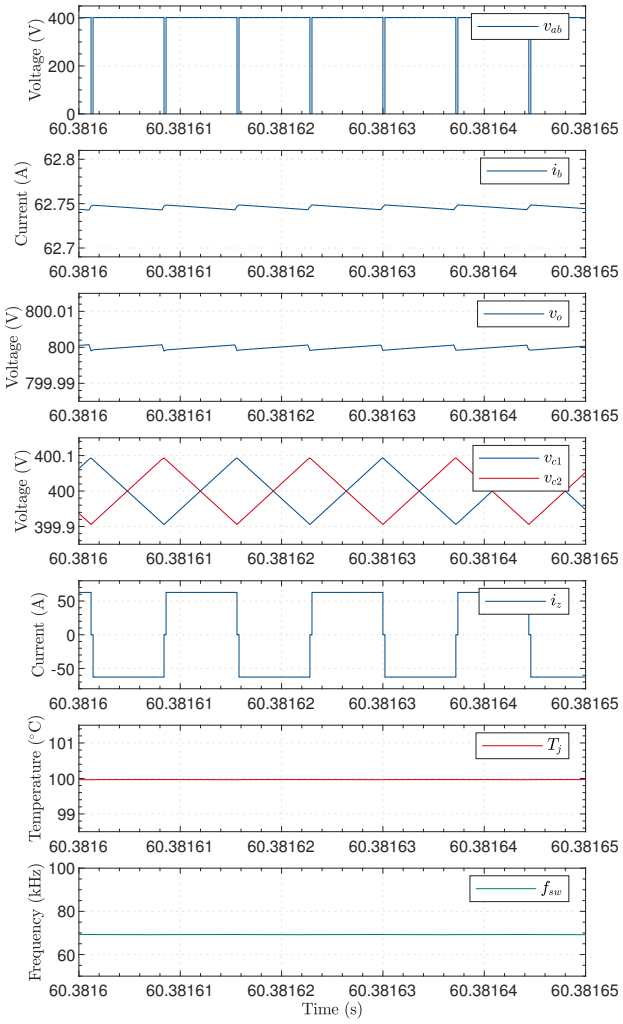

Fig. 12: Simulated steady state results for electrical and thermal variables of the TLBBC.

point current has a mean value $\bar{i}_z = 0$ A, and capacitor voltages v_{c1} and v_{c2} present a 180° shift.

V. Conclusion and Future Work

This paper presents a three-level buck-boost converter based on GaN HEMT semiconductor and presents control schemes for output voltage, voltage balance and junction temperature, which are implemented through classical linear PI controller.

The main contribution of this paper is the development of a high-power density converter for powertrain application in EVs, which incorporates an active thermal control scheme in order to mitigate the complete converter thermal stress. Furthermore, the effectiveness of proposed control schemes have been verified through comprehensive simulation results.

Finally, future work for this paper contemplates the study of the converter buck mode and a bi-directional test under mission profile of an EV, in addition to a battery model. Experimental verification of the converter with the proposed complete control scheme will be also shown in a future work.

Acknowledgment

This work was supported by ANID/PAI/SIA 2018/PAI77180032, by ANID-Basal Project FB0008 and by ANID/FONDAP/15110019 (SERC Chile).

References

[1] IEA, "Global EV Outlook 2020," 2020. [Online]. Available: https://www.iea.org/reports/global-ev-outlook-2020

[2] H. Tu, H. Feng, S. Srdic, and S. Lukic, "Extreme Fast Charging of Electric Vehicles: A Technology Overview," *IEEE Trans. Transport. Electrific.*, vol. 5, no. 4, pp. 861–878, 2019.

[3] A. Khaligh and M. D'Antonio, "Global Trends in High-Power On-Board Chargers for Electric Vehicles," *IEEE Trans. Veh. Technol.*, vol. 68, no. 4, pp. 3306–3324, 2019.

[4] S. Rivera, R. Lizana, S. Kouro, T. Dragicevic, and B. Wu, "Bipolar DC Power Conversion: State-of-the-Art and Emerging Technologies," *IEEE Trans. Emerg. Sel. Topics Power Electron.*, pp. 1–1, 2020.

[5] A. Taylor, J. Lu, L. Zhu, K. Bai, M. McAmmond, and A. Brown, "Comparison of SiC MOSFET-based and GaN HEMT-based high-efficiency high-power-density 7.2 kW EV battery chargers," *IEEE Trans. Power Electron.*, vol. 11, no. 11, pp. 1849–1857, 2018.

[6] GaN Systems Inc., "GS66516B 650 V E-mode GaN transistor Datasheet," 2020. [Online]. Available: https://gansystems.com/wp-content/uploads/2020/04/GS66516B-DS-Rev-200402.pdf

[7] Transphorm Inc., "TP90H050WS 900V Cascode GaN FET in TO-247 Datasheet," 2020. [Online]. Available: https://www.transphormusa.com/en/document/datasheet-tp90h050ws/

[8] GaNPower International Inc., "GPIHV30DDP5L N-channel 1200V30A GaN Power HEMT in TO263-5L Package Datasheet," 2020. [Online]. Available: http://iganpower.com/wp-content/uploads/2019/09/GPIHV30DDP5L_prelim_v2.pdf

[9] J. L. Lu and D. Chen, "Paralleling GaN E-HEMTs in 10kW–100kW systems," in *2017 IEEE Appl. Power Electron. Conf. Expo. (APEC)*, 2017, pp. 3049–3056.

[10] X. Jia, C. Hu, S. Du, M. Chen, P. Lin, and D. Xu, "DC-link voltage control strategy of a bi-directional DC/DC converter for electric vehicles," in *2015 IEEE Energy Conv. Congr. Expo. (ECCE)*, 2015, pp. 92–99.

[11] L. Tan, B. Wu, V. Yaramasu, and S. Rivera, "Effective voltage balance control for three-level bidirectional dc-dc converter based electric vehicle fast charger," in *2015 IEEE 10th Conf. Ind. Electron. Appl. (ICIEA)*, 2015, pp. 357–362.

[12] A. Soldati, F. Dossena, G. Pietrini, D. Barater, C. Concari, and F. Iannuzzo, "Thermal stress mitigation by Active Thermal Control: Architectures, models and specific hardware," in *2017 IEEE Energy Conv. Congr. Expo. (ECCE)*, 2017, pp. 3822–3829.

[13] M. Andresen, K. Ma, G. Buticchi, J. Falck, F. Blaabjerg, and M. Liserre, "Junction Temperature Control for More Reliable Power Electronics," *IEEE Trans. Power Electron.*, vol. 33, no. 1, pp. 765–776, 2018.

[14] R. Hou, Y. Shen, H. Zhao, H. Hu, J. Lu, and T. Long, "Power Loss Characterization and Modeling for GaN-Based Hard-Switching Half-Bridges Considering Dynamic on-State Resistance," *IEEE Trans. Transport. Electrific.*, vol. 6, no. 2, pp. 540–553, 2020.

[15] P. Kumar Prasobhu, V. Raveendran, G. Buticchi, and M. Liserre, "Active Thermal Control of GaN-Based DC/DC Converter," *IEEE Trans. Ind. Appl.*, vol. 54, no. 4, pp. 3529–3540, 2018.

[16] Y. Du, E. Aeloiza and R. Burgus, "INTERLEAVED MULTI-CHANNEL, MULTI-LEVEL, MULTI-QUADRANT DC-DC CONVERTERS," Patent US 2016/0 329 811 A1, Nov. 10, 2016.

[17] GaN Systems Inc., "GN002 Application Note - Thermal Design for GaNPX® Packaged Devices," 2020. [Online]. Available: https://gansystems.com/wp-content/uploads/2020/08/GN002-Thermal-Design-for-GaNPX-Packaged-Devices-Rev-200804.pdf

[18] P. Skarolek and J. Lettl, "GaN Transistors Cooling Options Comparison," in *2019 International Conference on Electrical Drives Power Electronics (EDPE)*, 2019, pp. 323–326.

[19] GaN Systems Inc., "GaN Systems Plecs Device Models," 2020. [Online]. Available: https://gansystems.com/plecs-device-models/

[20] L. Callegaro, M. Ciobotaru, D. J. Pagano, and J. E. Fletcher, "Control design for photovoltaic power optimizers using bootstrap circuit," *IEEE Trans. Energy Convers.*, vol. 34, no. 1, pp. 232–242, 2019.